ACS APPLIED BIO MATERIALS

www.acsabm.org Article

Graphene Microelectrodes for Real-Time Impedance Spectroscopy of Neural Cells

Amir Niaraki, Marilyn C. McNamara, Reza Montazami, and Nicole N. Hashemi*

Cite This: *ACS Appl. Bio Mater.* 2022, 5, 113−122 Read Online

ACCESS | Metrics & More | Article Recommendations | Supporting Information

ABSTRACT: Understanding the changes in the electrochemical properties of neural cells upon exposure to stress factors imparts vital information about the conditions prior to their death. This study presents a graphene-based biosensor for real-time monitoring of N27 rat dopaminergic neural cells which characterizes cell adhesion and cytotoxicity factors through impedance spectroscopy. The aim was to monitor the growth of the entire cell network via a nonmetallic flexible electrode array. Therefore, a water-based graphene solution was formulized as a conductive ink, 3D-printed into a flexible substrate through an electrohydrodynamic approach, resulting in electrodes with a conductivity of 6750 s/m. The presented high-throughput method enabled microscale monitoring of the entire cell network via the design of PDMS-based growth channels. The electrical resistance of the cell network was measured continuously along with their network density, constituting a mean density of 1890 cell/mm^2 at full cell confluency. The results demonstrate the applicability of the impedance-based sensing of the cell network for rapid screening of the cytotoxic elements, and the real-time effect of UV exposure on dopaminergic neural cells was reported as an immediate application of the device.

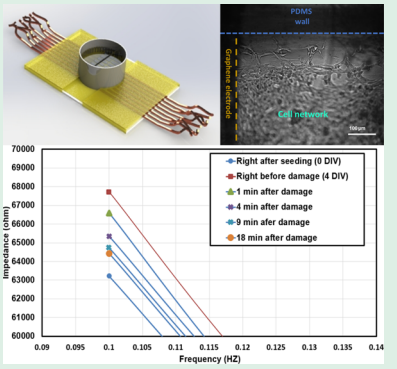

KEYWORDS: *aqueous graphene, flexible biosensor, microelectrode array, dopaminergic neural cells, impedance spectroscopy*

1. INTRODUCTION

The behavior of neural cells is dependent on the growth environment that they experience. Thus, manipulating the micrometer- and nanometer-scale attachment cues for these cells can assist the investigation of their electrical and optical properties in vitro.[1] Traditional patch clamp techniques provide high temporal resolution when obtaining single-cell electrical recordings. However, they have proven to be ineffective for monitoring the activity of large neural networks.[2] Therefore, electrical recording and stimulation of neural networks through nonpervasive extracellular microelectrodes has been the topic of extensive research.[3] Microfabrication of extracellular electrodes enables multiplexed detection of large cellular activities on a scale that is not achievable by micropipette technology.[4]

A major challenge, however, is to maintain a long-term connection between the soft cell tissue and the electrodes' conductive material, mainly due to the mechanical mismatch in the interface.[5−7] It is particularly valuable to determine whether the impedance change in a model cell culture under stress is reflected in the kinematics of cell death. Gold electrodes have been employed to detect the change in a local ionic environment caused by the cells' biological alterations.[8] For example, Diemert et al. studied the effect of impedance change in immortalized hippocampal neurons during the stages prior to their death with a gold electrode array.[9] Nevertheless, rigid metal-based electrodes can alter the cell shape, organization, and function of the cells, often leading to cytotoxicity and low cell viability.[10] Therefore, bilayer nanomesh[11] and indium tin oxide (ITO)[12] electrodes are reported as popular nonmetallic conductive materials, but these alternatives are naturally brittle. Moreover various in vitro studies on neuronal differentiation of stem cells[13] have showed that the stiff substrate alters the natural cellular behavior of neural cells. It is notable that the Young's modulus of the biological tissue in the central nervous system can range from 100 Pa to 10 kPa, while the widespread rigid silicon-based chips exhibit elastic moduli in the range of GPa.[14] In order to create a flexible platform, Adly et al.[15] created a carbon-based microelectrode array on PDMS and hydrogel. They further demonstrated the stimulation of cardiomyocyte-like HL-1 cells and recorded the membrane potential using this interface. Among other carbon-based materials, graphene has received growing attention for biointerfacing within drug delivery, bioassays, biosensors, and biological tissue scaffolding for applications such as stem cell growth.[16,17] There are numerous studies detailing neural attachment and the

Received: August 23, 2021
Accepted: December 23, 2021
Published: January 4, 2022

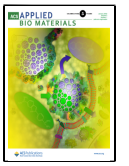

https://doi.org/10.1021/acsabm.1c00913
ACS Appl. Bio Mater. 2022, 5, 113−122

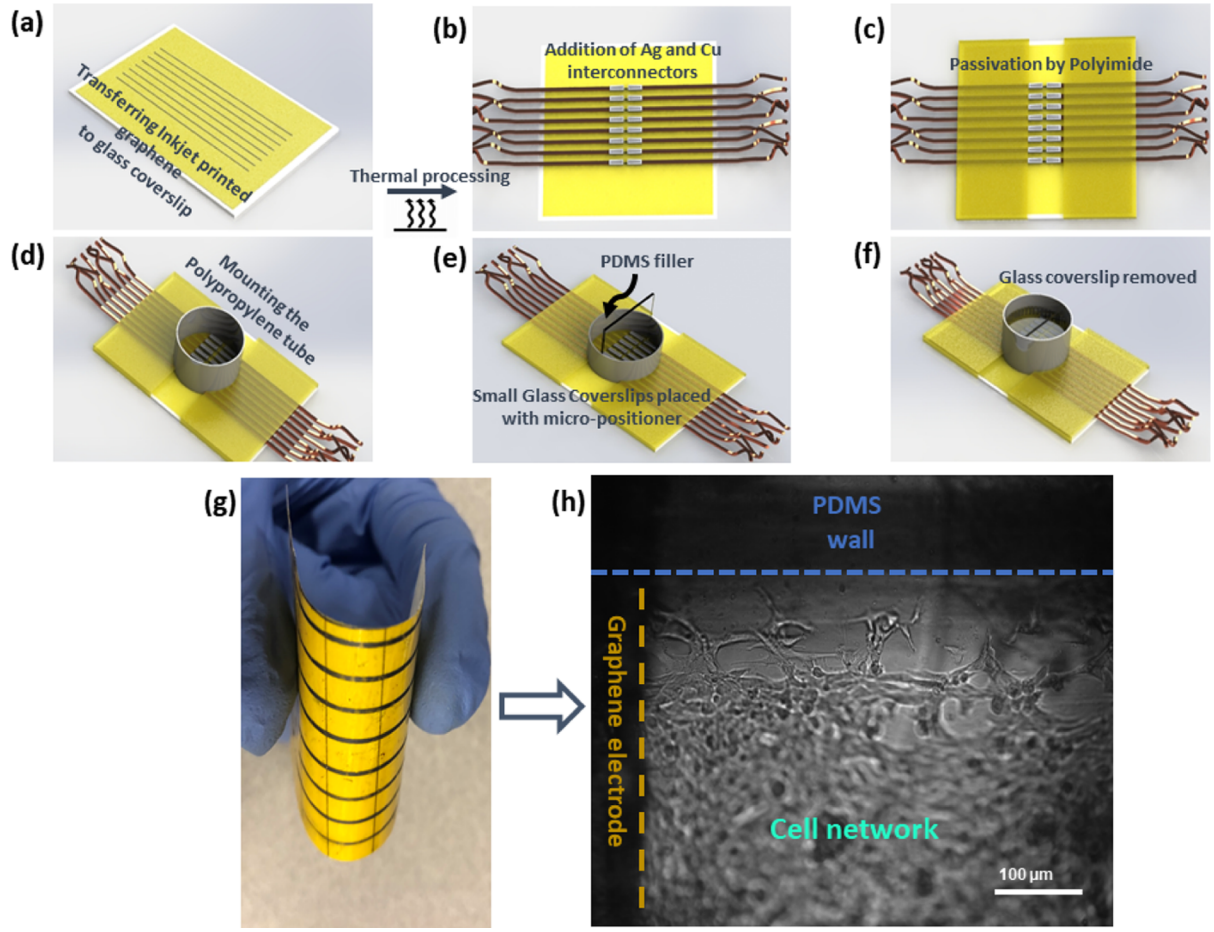

Figure 1. Fabrication of graphene biosensors for real-time monitoring of neural cells. (a) Transferring to a glass coverslip. (b) Addition of silver and copper for connection to the potentiostat. (c) Stabilizing the interconnectors with PI tape. (d) Mounting the cell container. (e) Creating the growth channel gap by micropositioning a glass slide. (f) Glass coverslip removal after PDMS hardening. (g) Flexible inkjet-printed graphene pattern prior to biosensor fabrication. (h) Proliferation of neural cells in the growth gap 5 days after interfacing with graphene microelectrodes.

capability of graphene to mediate cell growth and proliferation.[18] Herein, it is desirable to create a layered microstructure through inkjet printing of the water-dispersed graphene to more effectively detect the induced damage in neural cells. The microfluidic deposition of graphene electrodes can provide texture cues that are favored by the cells. Thus, the detection of cell detachment upon lift-off can be studied with high precision through the impedance spectroscopy technique, where the cell body is treated as a physical particle which impedes the transfer of ionic current between the electrodes in the growth media.

Cell impedance spectroscopy via such carbon-based materials is detailed in benchmark studies for cancer diagnosis.[19,20] Accordingly, inflicting cellular damage leads to alteration in membrane morphology, cellular shrinkage, detachment, and lift-off which will affect the cellular impedance.[9] With the aim of creating a real-time and continual monitoring platform for dopaminergic neural cells, here, a novel yet facile microfluidic approach is presented to fabricate a flexible graphene electrode array. Moreover, a PDMS-based passivation design is introduced to control the proliferation of N27 cells in the microscale and enable visual and electrical monitoring of the entire cell network by limiting the proliferation to a fully visible growth channel. This high-throughput design enables data acquisition in a larger scale, compared to the traditional end-point assays. Following our previous work,[21,22] aqueous graphene was synthesized by direct mechanical exfoliation of graphite with bovine serum albumin (BSA) through wet ball milling. It is known that BSA, among other proteins, can most effectively stabilize graphene platelets in water for biomedical purposes.[23−25] High concentration of graphene was dispersed in water through low-speed wet ball milling, which enhances the resulting conductivity of the electrodes after patterning.[26] The pure graphene solution was inkjet-printed on the treated polyimide (PI) substrate without the addition of metal nanoparticles, which are popular in graphene ink formulations,[27] followed by thermal treatment. We have found that employing a strong electrostatic field during the printing process can consolidate the graphene on the substrate. Therefore, the resultant microelectrodes could maintain their conductivity upon flexure without the addition of common insulating polymer binders such as ethyl cellulose.[28]

The quality of the graphene utilized in this study was characterized by its Raman spectrum, and transmission electron microscopy (TEM) and the surface morphology of the thermally treated graphene electrodes were examined by scanning electron microscopy (SEM). To quantify the flexibility of the sensor, resilience of the electrodes after bending and folding was tested for potential *in vivo* applications. The effect of stress factors (UV exposure here) on the electrical impedance and the viability of the N27 cell

https://doi.org/10.1021/acsabm.1c00913
ACS Appl. Bio Mater. 2022, 5, 113−122

culture were monitored continuously to demonstrate the dynamic applicability of the device as a sensitive alternative to dye-based techniques.

2. EXPERIMENTAL SECTION

The fabrication process of the biosensor from graphene patterns is depicted in Figure 1. First, the flexible substrate with printed graphene electrodes was transferred to 2″ × 3″ glass coverslips and was thermally annealed at 280 °C for 30 min. Afterwards, copper conductive tapes were attached to the graphene lines using Ag interconnectors and were fixed with a PI film to prevent detachment upon connection to the data acquisition system. In order to create the growth channel and ensure reliable cell growth, a 26 mm × 100 mm polypropylene tube (inner diameter × height) was mounted on the chip and sealed with polydimethylsiloxane (PDMS). A glass coverslip was placed perpendicular to the graphene lines via a micropositioner. The micro-positioning setup ensured a 4 μm vertical distance, from the substrate's surface to the tip of the glass coverslip. Subsequently, 5 mL of PDMS was poured in with a 10:1 base-curing agent ratio for electrode passivation. The chip was thermally annealed at 85 °C for 45 min in a convection oven and the glass slide was removed, leaving a channel width of 200 μm (for 0.17 mm-thick slides) or 1 mm (for standard 1 mm-thick slides). Prior to seeding, all chips were kept at room temperature overnight to ensure complete hardening of PDMS, followed by a wash-up with 70% ethanol, and a 30 min-long UV exposure in the culture hood.

2.1. Graphene Synthesis. A suspension of 20 mg/mL graphite (powder, <20 μm, synthetic, Sigma-Aldrich, catalog no. 282863) and 2 mg/mL BSA (lyophilized powder, Sigma-Aldrich, catalog no. A9418) was created in water. The suspension was ball-milled at low rotational speed (300 rpm) for 90 h with 11/32″ stainless-steel balls. The solution was then rested for ∼48 h to allow sedimentation of large graphite particles. 85% of the volume from the top was pipetted off to ensure the removal of Fe impurities. The resultant graphene concentration was controlled using a UV−vis spectrometer (PerkinElmer, Lambda 750).[21,25] In order to characterize the produced graphene, Raman spectra of the samples were acquired using a BWTEK Voyage confocal Raman system (B&W Tek, Newark, DE, USA), with a CW laser (Excelsior-532-150-CDRH Spectra-Physics) as the energy source operating at a wavelength of 532 nm. The aqueous graphene was drop-casted on Si/SiO_2 wafers with a drop diameter of ≈10 mm. The data were collected on five different laser spots across five independently printed electrodes and five untreated graphene samples (a total of $n = 30$) at a laser integration time of 10 s. The SEM images of printed graphene patterns on PI were captured via a JEOL FESM 6335 using 2−5 kV accelerating voltage. In order to prepare the graphene samples for TEM, they were diluted to 20 μg mL^{-1} and were drop-casted on a Cu grid. The TEM images were recorded using a JEOL JSM2100 STEM (Japan Electron Optics Laboratories, Mitaka, Tokyo, Japan) at 200 kV accelerating voltage. The impedance measurements were carried out using a VersaSTAT 4 Potentiostat Galvanostat. All electrical measurements were performed inside a grounded aluminum Faraday cage. For more details on graphene characterization, ink flow properties, and surface morphology tests (AFM, TEM, UV−vis spectroscopy, and profilometry), please refer to our previous work.[21,22]

2.2. Device Fabrication. A PI film 70 × 50 × 1 mm (length × width × thickness) was washed with acetone and isopropyl alcohol in an ultrasonic bath and blow-dried by compressed nitrogen. A polyimide film has a hydrophobic surface which requires surface modification for inkjet-printing. The PI film was initially submerged in a 12 mg/mL poly(4-styrenesulfonic acid) sodium salt (PSS) in deionized water for 20 min, followed by a submergence of 30 mg/mL polyethyleneimine (PEI) in water. PSS and PEI were purchased from Sigma-Aldrich (catalog no. 561959 and 408727, respectively). The water solvent contained a 0.5 M solution of NaCl prior to the addition of PEI and PSS. The substrate was rinsed with deionized water and thoroughly dried with compressed nitrogen before and after each submergence. The prepared graphene solution was then inkjet-printed on PI (0.06 mm thickness) using an electrohydrodynamic inkjet printer. Briefly, the graphene ink was deposited on the treated PI in a single pass with a syringe pump creating a constant flow regime (9 μL/s) with a 300 μm needle. The printing processes resulted in a finger thickness of 4 μm, a width of 450 μm, and a spacing of 900 μm. In order to ensure the binding of the graphene to the substrate, a constant electrostatic field was applied between the nozzle and the PI film. The consolidation of graphene patterns eliminated the need for binders such as ethyl cellulose[29] and lead to stability at the time of flexure. The distance between the tip of the nozzle and the PI was set to 1 mm, while the electrical potential applied via a function generator was 3.5 kV. The fluid and properties of the electrohydrodynamic process are detailed in the Supporting Information.

2.3. Electrochemical Characterization. Cyclic voltammetry (CV) was performed via a potentiostat in a three-electrode cell setup (PerkinElmer 4). A solution of 1 M KCl (≥99% Sigma-Aldrich) was prepared in DI water as the electrolyte. Pt wire was employed as a counter electrode, and a Ag/AgCl electrode was submerged for a reference electrode. The CV measurements were conducted to determine the Faradaic peaks, in a potential range of −1 to 1 V with respect to the Ag/AgCl electrode at a scan rate of 100 mV/S.

Electrical impedance spectroscopy (EIS) was performed in a three-electrode setup with the same potentiostat. For the electrode characterization tests given in SI, phosphate-buffered saline (PBS) was used as the electrolyte solution and Pt wire and Ag/AgCl electrode served as the counter and reference electrode. The frequency was scanned from 10 kHz to 0.1 Hz with $V_{DC} = 0$ and $V_{AC} = 10$ mV. Both EIS and CV were performed in a grounded aluminum mesh, serving a Faraday cage and were repeated for five electrodes on four separately fabricated chips ($n = 20$). In order to study the effect of cytotoxicity on the cell culture, the UV light was emitted via a Dymax BlueWave 200 version 3.0 light-curing spot-lamp system in 20 s intervals with an intensity of 40 W/cm^2.

2.4. Cell Culture and Biocompatibility Analysis. The growth channels were designed to control the expansion of the cell network and facilitate the adhesion of neural cells to the topological features of the graphene lines.[30] Therefore, a concentrated suspension of N27s in the growth medium (GM) was initially introduced to the growth channel to ensure the deposition of the cells only on the electrode area. The GM contained RPMI medium 1640 (1×), 10% fetal bovine serum (FBS), 1% penicillin, and 1% L-glutamine. For all trials, cells were cultured in T-25 flasks at 70% confluency and were passaged at least three and no more than ten times prior to their introduction to the chips. In two day intervals, half of the volume of cultured cells was replaced by fresh GM. The N27 cells were detached for passage using 0.025% trypsin−EDTA. The cell suspension was centrifuged at 1500 rpm for 5 min and after the removal of trypsin-containing medium, it was resuspended in fresh GM. A Trypan blue (Gibco BRL) viable cell count was performed before the cell passage to the chips with a medium-to-dye ratio of 1:9.

A total of 50 μL of cell suspension was added to the growth channels with a size of 0.2 mm × 26 mm × 5 mm (for width × length × depth). Six hours after the cell passage, an additional 2 mL of GM was added and the chip was incubated at 37 °C in a 5% CO_2/95% humidified air atmosphere for 5 days.

The biocompatibility of the chips was analyzed via a standard live−dead cell assay using a 70 μM CellTracker CMFDA solution and an 80 μm propidium iodide solution in FBS-free RPMI medium. A total of 50 μg of CellTracker was dissolved in 10.8 μL of dimethyl sulfoxide (DMSO) to prepare the 70 μM CellTracker CMFDA solution, prepared using FBS-free RPMI medium. A total of 500 μL of the prepared dye was added to the chip before incubating for 30 min. Subsequently, the dye was replaced by FBS-free RPMI medium after incubation to maintain the samples' moisture during imaging. For the introduction to chips and viability test, all cell detachments were performed with 0.05% trypsinEDTA (Ginco BRL). The live−dead cell assay results were gathered using a Zeiss Axio Observer Z1 inverted microscope. During all the experiments, the dyes were covered to prevent their exposure to light. The microscope was set to capture green excitation/emission spectra (492/517 nm maxima) for

https://doi.org/10.1021/acsabm.1c00913
ACS Appl. Bio Mater. 2022, 5, 113−122

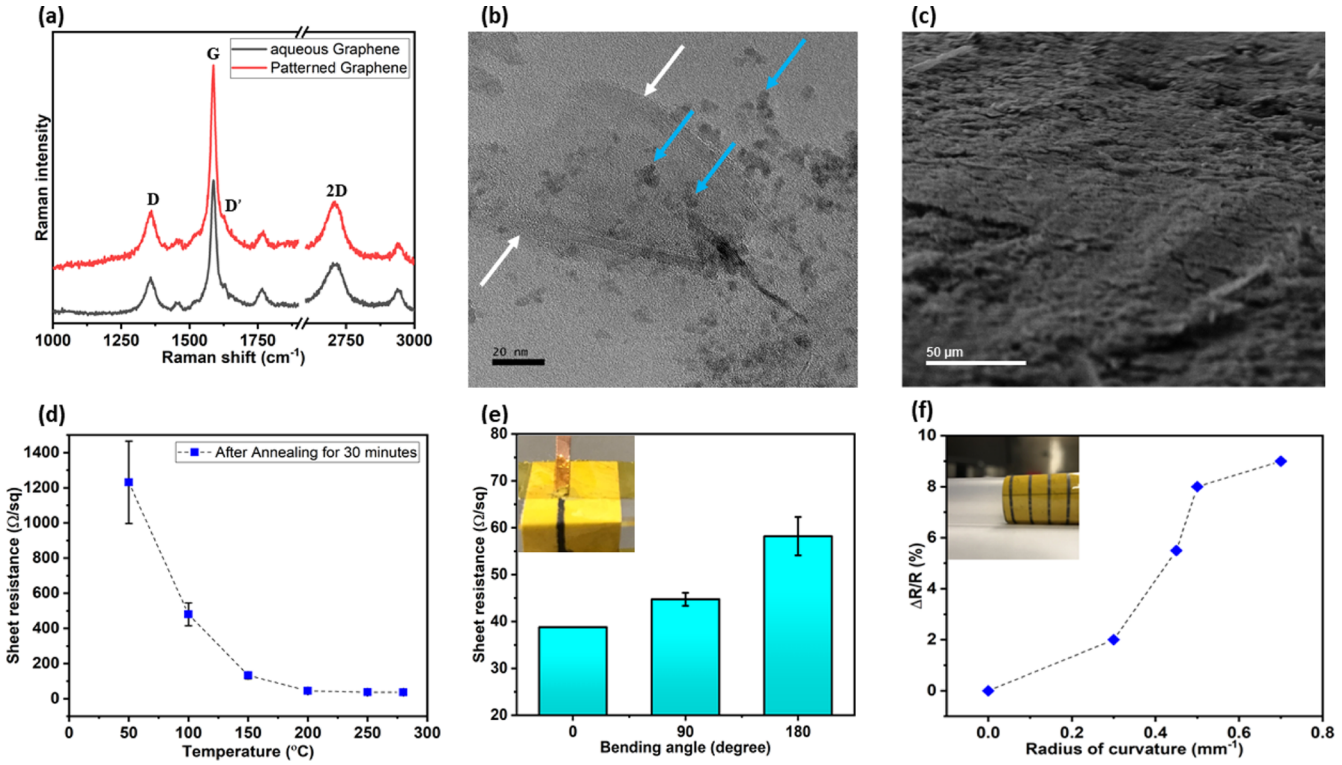

Figure 2. Characterization of aqueous graphene ink before and after patterning. (a) Raman spectra of aqueous graphene and treated graphene electrodes acquired at λ = 532 nm. (b) TEM imaging of graphene platelets in water. The graphene nanosheets are shown with white arrows and BSA nanoparticles are shown with blue arrows. Scale bar: 20 μm (c) SEM imaging of annealed graphene electrodes. Scale bar: 50 μm. (d) Reduction in sheet resistance of the shear-exfoliated graphene after 30 min of annealing in temperatures varying from 50 to 300 °C. (e) Change in the sheet resistance of 10 mm-long graphene lines after attachment to glass coverslips with respect to 90 and 180° folding angles. (f) Relative change in resistance of 20 mm-long graphene lines with respect to various radii of the curvature.

Table 1. Raman Analysis of Shear-Exfoliated Graphene before and after Inkjet-Printing and Thermal Processing[a]

graphene	D position (cm−1)	G position (cm−1)	G fwhm (cm−1)	2D position (cm−1)	2D fwhm (cm−1)	I_D/I_G
pre-treatment	1358 ± 0	1587 ± 1	17 ± 1	2700 ± 7	52 ± 7	0.25 ± 0.03
post-treatment	1357 ± 3	1587 ± 1	17 ± 3	2703 ± 2	52 ± 5	0.32 ± 0.04

[a]Results are presented as mean ± SD, across five independently fabricated electrodes and drop-casted aqueous graphene for five laser spots each (n = 30).

CellTracker CMFDA and red excitation/emission spectra (532/617 nm maxima) for propidium iodide. The viability was calculated with eq 1, where green refers to the live cells stained by CellTracker CMFDA and red refers to the dead cells stained by propidium iodide. The statistical analysis was performed using a two-sided student's test.

$$\text{Viability} = \frac{\text{Live cells(green)}}{\text{Live cells(green)} + \text{Dead cells(red)}} \times 100 \quad (1)$$

3. RESULTS AND DISCUSSION

The change in mechanical and electrical properties of graphene, from an aqueous ink to a postprocessed conductive pattern, requires vigilant examinations (Figure 2). Raman spectroscopy is the best source of information for investigating the structural integrity of the graphene samples.[31] The presence of lattice defects directly affects the vibrational frequencies of the carbon atoms and is detectable via Raman spectroscopy. Raman spectra of the aqueous graphene (drop-casted on Si/SiO_2 chips) and the thermally treated graphene electrodes are shown in Figure 2a. The comparison between the Raman spectra of aqueous graphene and the treated patterned graphene shows no significant dislocation of the peaks (Table 1). The presence of a short D band at 1357 ± 2 cm^{-1}, a sharp G band at 1587 ± 1 cm^{-1}, and a symmetric 2D band at 2700 ± 2 cm^{-1} with an FWHM of 52 ± 7 cm^{-1} is indicative of defect-free few-layer graphene with $\frac{I_D}{I'_D} = 1.2 \pm 0.2$.[32] Notably, the ratio of the intensity of D band to the D′ shoulder peak characterizes boundary defects ($I_D/I'_D > 3.5$), vacancy basal plane pint defects ($I_D/I'_D > 7$), and sp^3defects ($I_D/I'_D > 13$).[25] Prior to patterning, the suspension of graphene nanosheets in water was also examined via TEM imaging. Figure 2b demonstrates a single graphene platelet among BSA nanoparticles that enable their suspension in water. Owing to their few-nanometer thickness, the graphene nanosheets appear to be almost transparent.

3.1. Electrohydrodynamic Patterning of Graphene.

Since the produced graphene solution is ionically charged, surface modifications on the PI tape deemed vital to ensure the wettability of the substrate prior to the inkjet-printing process. The contact angle of the graphene ink decreased from 64 to 24° when dropped on the hydrophilic surface of the treated PI substrate, compared to the untreated tape (Figure S1).

https://doi.org/10.1021/acsabm.1c00913
ACS Appl. Bio Mater. 2022, 5, 113−122

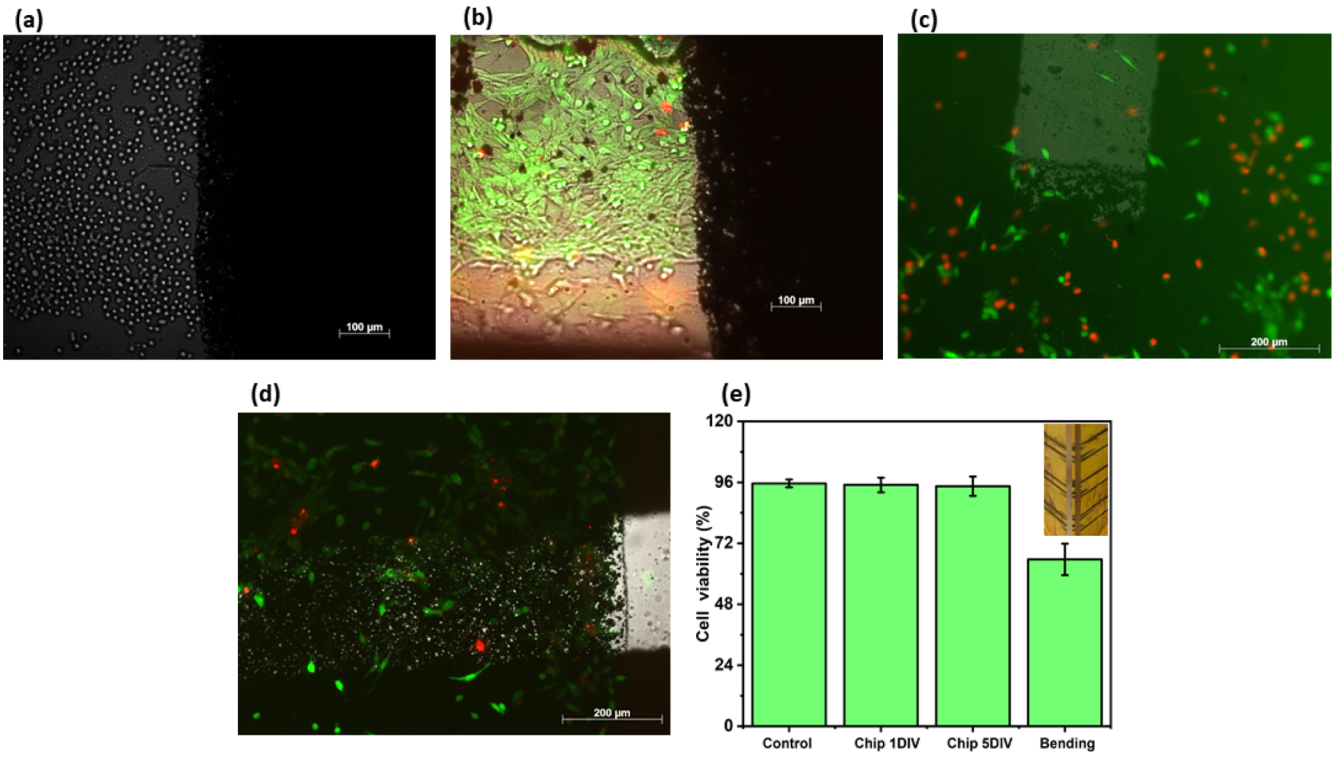

Figure 3. Cell adaptability on the biosensor. (a) N27 cells immediately after passage to the growth channel. (b) Cell viability after 5 days *in vitro*. (c) Live−dead cell assay after the cell growth in conjunction with the bending of the electrodes with a folding angle of 90°. (d) Live−dead cell assay after the removal of the PI substrate with the microchannel from the glass substrate. The electrodes in the growth channel were washed up with media and turned upside down for 5 min. The N27 cells surprisingly remained attached to the graphene lines but left the rest of the substrate area during the wash-up. (e) Thorough cell viability test for the biochip, the control, and the bent electrode array with a folding angle of 90, reported as mean ± standard deviation over one control, four independent chips (n = 15). One-way ANOVA $p < 0.005$.

Traditionally, graphene ink formulations contain polymers such as ethyl cellulose to ensure their binding to the substrate during the thermal processing. It should be noted that the overall conductivity of graphene patterns are hindered with the appearance of microscale cracks during the thermal processing or flexure, more than the size of the nanosheets. Polymer binders, although naturally insulating, are typically essential to maintain the microscale integrity of the printed lines. In order to bypass the need for the stabilizing binders and avoid numerous printing passes, here, an electrostatic field was applied during the jetting processes to consolidate the graphene patterns on the PI substrate.

The fluid dynamics of the jetting process is modeled through the benchmark work of Fromm, where a dimensionless grouping of the Reynolds and Weber was used to solve the Navier−Stokes equation set (Supporting Information).[33] Briefly, eq 2 defines the Ohnesorge number Z, where if it is too small, the velocity is the dominant parameter and thus a large positive pressure is required for droplet ejection leading to low velocity and short fluid column extension. In contrast, a high value of Ohnesorge number constitutes a long fluid column leading to the satellite drop formation behind the main drop.[34] Typically, the Z value for highly loaded particulate suspensions should be between $0.1 < Z < 1$ and was shown to be equal to 0.23 for the inkjet-printing method that was used in this study. Fluid properties are also important for determining the resultant resolution of the patterns upon droplet impact. Similar to the Ohnesorge number, a generally accepted parameter for describing the splashing of droplets is given using eq 3 where a high K value should be set to lower values than 100. When this dimensionless grouping of Reynolds and Weber number exceeds this critical threshold, splashing may be observed depending on the temperature and substrate conditions. Parametric modeling of the graphene ink and the electrojet setup constitute an Ohnesorge value of $Z = 0.23$ and a drop impact of $K = 12.99$, as detailed in the Supporting Information.

$$Z = \frac{(We)^{0.5}}{Re}; \qquad 0 < Z^{-1} < 10 \tag{2}$$

$$K = We^{0.5}Re^{0.25}; \qquad K < 100 \tag{3}$$

Thermal processing promotes the adhesion of graphene ink to the substrate while enhancing the electrochemical properties of the electrode through release of possible oxide compounds that may have been introduced during the ink formulation and printing process.[4] Moreover, the SEM imaging (Figure 2c) can show that the surface morphology of thermally annealed electrodes with layered stack of carbon films which can provide a desirable scaffold for neural adhesion.[35] As demonstrated in Figure 2d, sheet resistance of the printed lines dropped from 1200 to 37 Ω/sqr upon 30 min of annealing in 280 °C. Therefore, the equivalent conductivity of an electrode with a cross-sectional size of 450 × 4 $(\mu m)^2$ reached 6750 S/m.

3.2. Flexibility Analysis. In order to investigate the limits on the flexibility of the electrodes, the change in their resistance upon bending was studied, together with silver conductive ink and copper tape as the interconnection setup. While the curvature of the substrate affects the resistance of the lines minimally, sharp folding of the electrodes can introduce

https://doi.org/10.1021/acsabm.1c00913
ACS Appl. Bio Mater. 2022, 5, 113−122

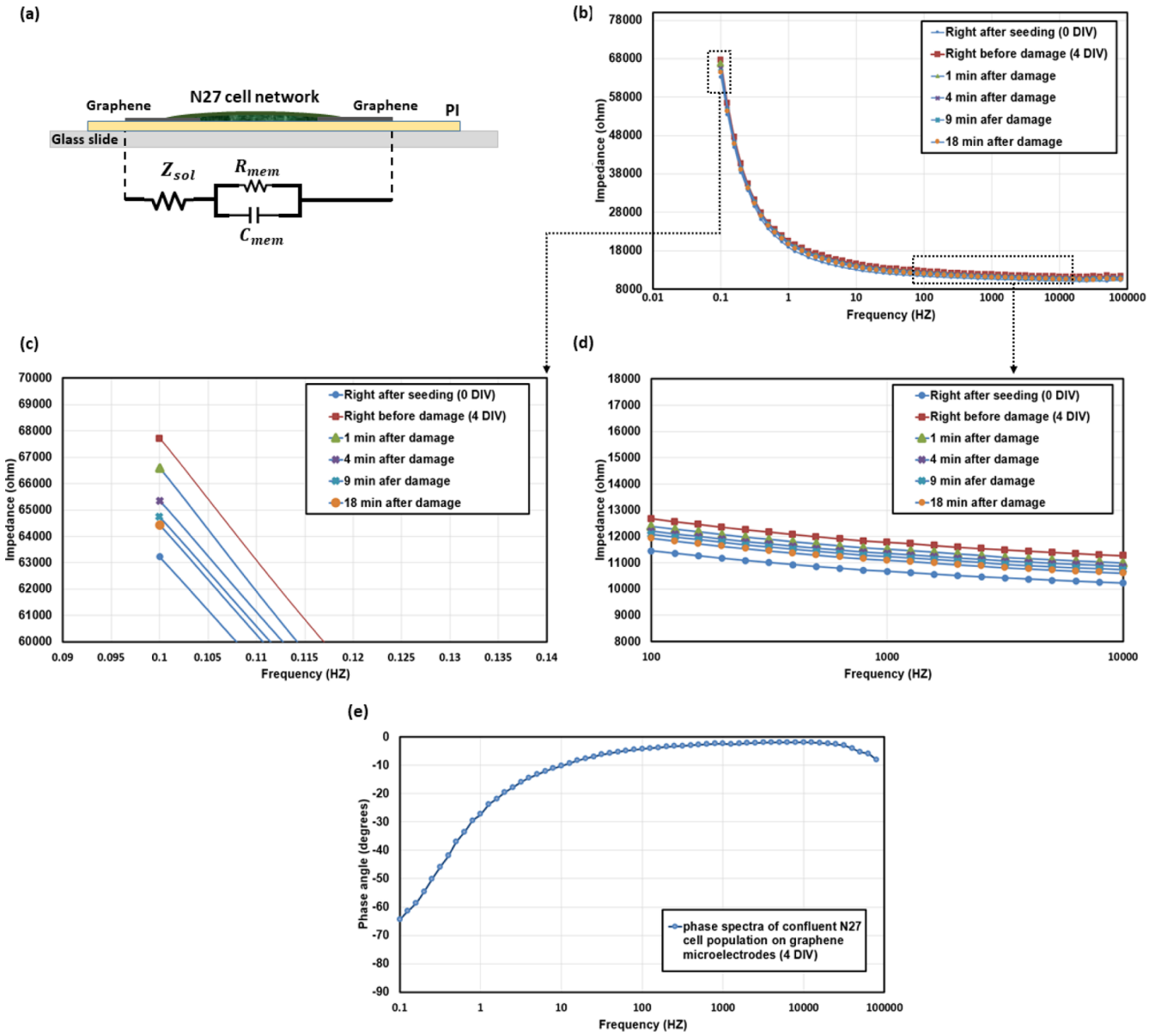

Figure 4. Impedance spectroscopy of N27 cell culture on graphene microelectrodes. (a) Overview of a simplified equivalent circuit. (b) Sample impedance spectrum in frequencies ranging from 0.1 Hz to 100 kHz for the electrodes at rest, electrodes under confluent N27 cell population, and after undergoing damage (UV exposure). (c) Electrical impedance between graphene microelectrode pairs in the low-frequency regime (0.1 Hz). (d) Electrical impedance spectrum in the high-frequency regime, ranging from 100 Hz to 10 kHz. (e) Phase spectra of confluent N27 cell population on graphene microelectrode arrays after 4 DIV.

microscale cracks (Figure 2e,f). In the trials on 20 electrodes, no case of absolute line disconnection was observed, but the average sheet resistance increased from 37 to 58 Ω/sqr after sharp 180° folding.

With flexible electrodes in hand, we are interested in the level of adhesion of neural cells to the graphene interface. Figure 3 shows the density of N27 cells in the biochip throughout the experiments. Controlling the growth area of the cells is a major need for monitoring the entire cell network.[1]

3.3. N27 Cell Adherence. Hence, the six hour gap between the initial passage of the cells into the growth gap (Figure 3a) and the final addition of GM was observed to be crucial for limiting the cells' mobility. A concentration of 2.55 × 10^6 cells/mL was cultured on the chips and the resulting cell densities were monitored for 5 days in vitro (DIV) with the resultant cell viability demonstrated in Figure 3. It is observed that flexure of the electrodes after cell growth with a folding angle of 90° can result in a drop in cell viability to 66% (Figure 3c,e). However, the cells in the control and in the growth enabled a cell viability of >95%. Thus, it can be concluded that the shear-exfoliated graphene microelectrodes and the created growth channel induced no detectable cytotoxicity.

Impedance spectroscopy has been widely used to assess the growth of neurons, cancer cells, and microbial biofilms and to characterize the physical processes at the electrode−biomaterial interface because it is a fast, sensitive, and label-free technique.[36] When an electrostatic field is created between two electrodes submerged in ionic media, the cell body acts as insulating particles that impede the flow of the electric current at the cell−electrode interface, resulting in a measurable increase in the impedance. Therefore, the adhesion degree of

https://doi.org/10.1021/acsabm.1c00913
ACS Appl. Bio Mater. 2022, 5, 113−122

the biological tissue to the interface material plays a key role in translating the damage intensity to the impedance as the sensing parameter. Figure 3d demonstrates that the N27 cells favor the surface morphology of the graphene pattern and show a significant detachment degree. We have peeled off the PI substrate and washed the growth channel with media after cell staining and surprisingly observed that although the cells were fully washed on the clear substrate spots, many N27 cells remained attached to the graphene pattern.

In order to examine the level of cell attachment to the graphene electrodes, the electrical impedance of the electrodes both prior to and immediately after cell passage was tracked, as well as 1 to 5 times in each DIV thereafter until the cell network reached its maturity. Here, we define the network maturity by a cell density of >1500 cells/mm^2. In most of the trials, the cell network reached the desired density after three DIV. Real-time optical and electrical monitoring of the cell behavior was enabled throughout the entire growth channel. Since the system could not be integrated in the incubator, repetitive rotation of the biochip in and out of the incubator appeared to be inevitable. See Figure S3 for annotated components of the real-time monitoring of the cell network and Figure S4 for CV and EIS characterization of the cell-free electrodes in KCl and PBS.

3.4. Measuring the Effect of Damage on Neural Cells.

To induce the stressor, the cells were exposed to a high-intensity light-curing spot-UV-lamp system for 20 s. The exposure of N27 cells to 40 W/cm^2 of UV light leads to almost immediate cell shrinkage and lift-off. We are interested in measuring the change in electrical impedance of each electrode right before and after the UV exposure. The equivalent circuit is presented in Figure 4, adapted from the benchmark studies for cancer diagnosis via impedance measurements,[19] where C_{mem} refers to the lipid bilayer and R_{mem} represents the ion channels in the cell network.[19] The impedance of the ionic growth medium is shown by Z_{sol}.

Generally, within an individual cell, the cytoplasm is the conductive region with conductance of one million times more than the cells' membrane.[19] Thus, the cell membrane lipid bilayer constitutes to the dominant capacitive component of the cell culture in the high-frequency regime (C_{mem} in Figure 4a). Figure 4b demonstrates a sample reading of the microelectrode setup, for 0 to 4 DIV and after exposure of the cells to the stressor. When the cells grow on conductive microelectrodes, their membrane acts as insulating particles. Therefore, the alternating current voltage over a range of frequencies generates an electrostatic field which is impeded by these cell bodies. Hence, the multiplexed detection of cell growth and adhesion can be quantified by measuring the added impedance between the graphene microelectrode pairs.

Figure 4d demonstrates that in higher frequencies, when the electrodes are at rest in the ionic growth media before cell attachment, the electrical impedance between graphene electrode pairs is at its minimum value of 11 452 Ω at 100 Hz, 10 671 Ω at 1000 Hz, and 10 222 Ω at 10 000 Hz. The impedance of the same electrode pair after complete growth of the cell population on 4 DIV reached its maximum value of 12 683 Ω at 100 Hz, 11 782 Ω at 1000 Hz, and 11 269 Ω at 10 000 Hz. The impedance spectrum at 1, 4, 9, and 18 min after exposure to UV suggests gradual detachment and lift-off of N27 cells from the surface of graphene electrodes which allows an increase in the ion transfer rate resulting in a continuous reduction in impedance values in the high-frequency regime.

It should be noted that despite the availability of electrodes' impedance at any moment after seeding, the impedance of the cell population prior to the maturity of the network may not be reliably calculable. Nevertheless, owing to the layered surface morphology of graphene electrodes, we observed that the N27 cell network fully adheres to the lines, and 100% confluence is achievable even after 1 DIV and consistently after 3 DIV. For instance, the behavior curve in 1 DIV demonstrates only a minimal difference when compared to the curve for 3 DIV. Overall, the microscale biological status of the cell−graphene interaction affects the measured impedance as a consequence of constant modification of the ionic environment around the electrodes. Thereby, in addition to cell viability which is observable through optical methods; the cell number, morphology, and adhesion degree can be determined by utilizing the multiplexing functionality of the microelectrode array. The real-time monitoring of the N27 neural cells is achieved by repetitive impedance spectroscopy of the graphene microelectrodes. In order to enable repeatable monitoring of the cell network, the impedance value obtained from multiplexing between the adjacent electrode pairs is normalized as a dimensionless parameter, resistance index (RI), given in eq 4

$$\mathrm{RI}_i = R_{\mathrm{cell}}(t_i)/R_{\mathrm{init}} \tag{4}$$

where, at any measurement time instance t_i, the end-to-end time-dependent measured impedance of the cells $R_{\mathrm{cell}}(t_i)$ is divided by the initial impedance between of the electrode pairs with media before cell adhesion R_{init}. Figure 5 demonstrates the change in RI across multiple samples for instances

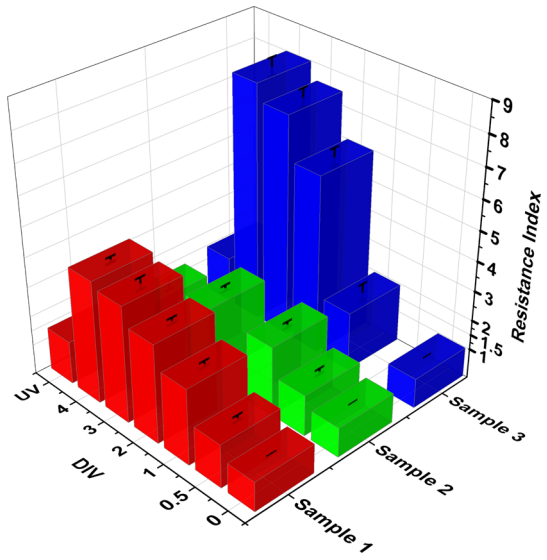

Figure 5. RI for three samples of N27 neural population. The impedance between the graphene electrode pairs during the cell network maturity (>1500 cells/mm^2) and post UV exposure was normalized with respect to the impedance between the electrodes right after seeding. The growth rate of the cell network and their resultant confluence determines the RI across the electrodes deposited in the growth channels. The rapid growth of the index deaccelerates upon the network's maturity. Upon exposure to UV, the cell impedance of samples 1−3, respectively, drops to 1.44, 1.32, and 1.55 of the initial impedance value between the graphene electrodes. This impedance drop represents cell shrinkage and lift-off due to cytotoxicity. The cell density between each electrode pair determines the value of the index on that particular electrode−cell interface.

https://doi.org/10.1021/acsabm.1c00913
ACS Appl. Bio Mater. 2022, 5, 113−122

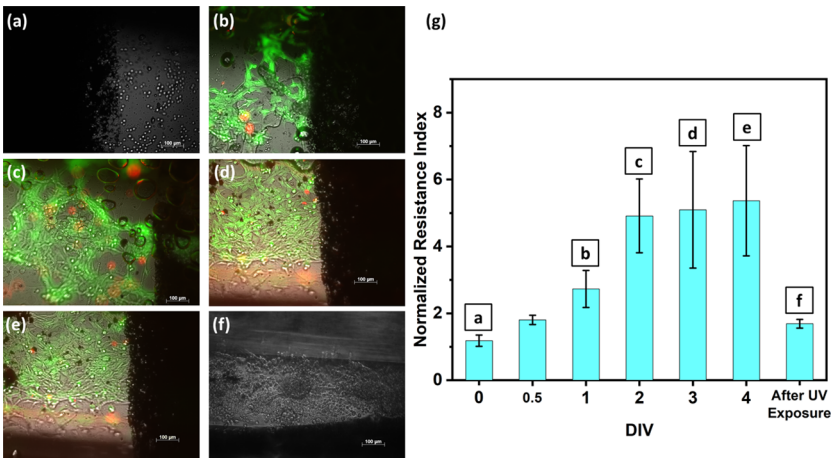

Figure 6. Optical microscopy images of the N27 cell network in four days after passage (left) and the corresponding normalized cell index (right). (a) Freshly passaged cells. The sample image of the cell network after (b) 1 DIV, c) 2 DIV, (d) 3DIV, (e) 4 DIV, and (f) after 20 s exposure to UV light; scale bar 100 μm. (g) Normalized RI presented in terms of mean ± standard deviation across five independent chips, monitored 1−5 times per day for four DIV followed by UV exposure (n = 60). After normalizing the RI with respect to the cell density, the NRI can enable real-time monitoring of the entire neural cell population prior and after to UV exposure. Upon the neural network's confluency (by 3DIV), the cell density across all experiments can be given as 1890 ± 230 cells/mm^2.

immediately after seeding to day 4 where the networks were exposed to UV light all measured at a low frequency of 0.1 Hz. Although in every trial RI reaches to a relatively constant value upon full confluence, the resultant RI is highly dependent on the cell density and the particular cell formation around the electrodes. Nevertheless, exposure to UV results in cell shrinkage and lift-off which in turn results in a reduction in the electrode−membrane interface area and extreme reduction of RI as the electrodes can be exposed to the ionically charged medium.

In order to generalize the analysis, the cell density was visually monitored at the time of impedance measurement to give the normalized RI of the cell network (NRI) given in eq 5, where σ_i gives the lateral cell density in cell/mm^2 at any measurement instance.

$$\mathrm{NRI}_i = \mathrm{RI}_i/\sigma_i \tag{5}$$

The idea is to enable the dynamic monitoring of real-time neural responses to the stress factors without the dye assays. Although the exact time frame in which the cell network reaches to full confluence may vary from chip to chip, optical measurement of cell density along with electrical spectroscopy can result in NRI which can represent the cell adhesion degree and networks' real-time viability without the need for repetitive fluorescence assays. Figure 6 demonstrates that upon maturity of the cell network (σ_i > 1500 cell/mm^2), the NRI remains steady at around 4.5 times of its initial value across all covered electrodes. This value drops to an average of 1.45 when the introduction of the cytotoxic factor leads to cell shrinkage and contraction of the network (Figure 6f). It is worth noting that defining a measure for cell density after complete death of the network did not seemed possible as the cells slowly start to raise in medium, while a small portion of them appear to be entrapped by the body of the electrode. This partial entrapment along can be the cause of the remaining discrepancy in the NRI before the seeding and eventual impedance upon the lift-off. The effect can also be observed in Figure 4d, where the V−I curve of the cell network after the UV exposure does not completely follow the Ohm law. The preference of the cell network for adhering to the electrodes as opposed to the PDMS−substrate corners could be a result of utilizing few-layer aqueous graphene as the working material. Throughout the in vitro studies on neural cells, it is commonly reported that[37−39] cultured cells often aggregate in the corners or the trenches of the microchannel systems due to the presence of textural cues.[40] Accordingly, the layered structure of the inkjet-printed graphene electrodes can be suitable for cell attachment which is vital for establishing a stable communication pathway in the cell−electrode interface (Figure 3d). The accuracy of the presented method is highly reliant on the fact that the entire body of the network could be monitored owing to the narrow growth channels. Nevertheless, vertical aggregation of the cells appears to be inevitable which was shown to have a minimal effect on the NRI but can hinder the cell density measurement and can be considered as a source of error for the monitoring system. This was one motive for conducting the experiments on the effect of stress factors no later than 5 DIV. We believe that real-time impedimetric monitoring of the N27 cells was enabled by the wrinkled surface morphology of the graphene electrodes which provided the proper attachment cues for the cell population. Such a scaffold subsequently played a prominent role at the time of the gradual detachment of the cells from the surface of the biosensor and aided the minute-sensitive impedimetric monitoring of neural death.

Overall, the effect of stress factors on the NRI of the dopaminergic cells can be considered as an immediate application of the proposed system. In particular, the N27 cell line is a common model for Parkinson's disease and has been a subject of investigation for understanding neurotoxicity and oxidative stress factors in numerous studies. The flexibility of the electrode array can suggest further applicability of the framework for future *in vivo* studies.

4. CONCLUSIONS

Presented here is a graphene-based biosensor that is easily made and capable of *in vitro* impedimetric monitoring of the cell network in real-time. The abundantly available cell assays are normally pervasive and can provide information only for defined end point measurement. The inkjet-printed electrodes

https://doi.org/10.1021/acsabm.1c00913
ACS Appl. Bio Mater. 2022, 5, 113−122

were equipped with microfluidic design of growth channels to control the growth of the cell network. Doing so, enabled real-time optical monitoring of the entire cell network along with electrical spectroscopy. As a proof of concept, the N27 cells were passaged in the microchannel, grew until network maturity, and exposed to UV as the cytotoxic element, and the change in their RI and density was reported at every stage during this period. The water-based graphene electrodes can show resilience from bending and folding without the addition of polymer binders and could maintain their high conductivity with the presence of no metal nanoparticles. This can suggest the potential use of the presented method for future in vivo studies. Moreover, adhesion of the cell network to the graphene electrodes was demonstrated and an average cell density of 1890 cells/mm^2 was resulted along with a rapid 100% cell confluency on the presented microelectrode interface.

■ ASSOCIATED CONTENT

Supporting Information

The Supporting Information is available free of charge at https://pubs.acs.org/doi/10.1021/acsabm.1c00913.

Image of contact angle of graphene on treated and untreated PI; electrojet-printed graphene microelectrodes under flexure; all the components of the cell monitoring setup; and electrochemical characterization of cell-free electrodes (PDF)

■ AUTHOR INFORMATION

Corresponding Author

Nicole N. Hashemi − *Department of Mechanical Engineering, Iowa State University, Ames, Iowa 50011, United States; Department of Mechanical Engineering, Stanford University, Stanford, California 94305, United States;* orcid.org/0000-0001-8921-7588; Email: nastaran@iastate.edu

Authors

Amir Niaraki − *Department of Mechanical Engineering, Iowa State University, Ames, Iowa 50011, United States*

Marilyn C. McNamara − *Department of Mechanical Engineering, Iowa State University, Ames, Iowa 50011, United States*

Reza Montazami − *Department of Mechanical Engineering, Iowa State University, Ames, Iowa 50011, United States;* orcid.org/0000-0002-8827-0026

Complete contact information is available at: https://pubs.acs.org/10.1021/acsabm.1c00913

Author Contributions

The manuscript was written through contributions of all authors. The authors have given approval to the final version of the manuscript.

Notes

The authors declare no competing financial interest.

■ ACKNOWLEDGMENTS

This work was partially supported by the Office of Naval Research Grant N000141712620 and the National Science Foundation Award 2014346. The authors acknowledge Mehran Abbasi Shirsavar, Nicholas Hunter, and Kelli Williams for the technical help in characterization tests and Alexander Knapp for illustration.

■ REFERENCES

(1) Hanson, J. N.; Motala, M. J.; Heien, M. L.; Gillette, M.; Sweedler, J.; Nuzzo, R. G. Textural Guidance Cues for Controlling Process Outgrowth of Mammalian Neurons. *Lab Chip* **2009**, *9*, 122−131.

(2) Spira, M. E.; Hai, A. Multi-Electrode Array Technologies for Neuroscience and Cardiology. *Nat. Nanotechnol.* **2013**, *8*, 83−94.

(3) Wise, K. D.; Angell, J. B.; Starr, A. An Integrated-Circuit Approach to Extracellular Microelectrodes. *IEEE Trans. Biomed. Eng.* **1970**, *17*, 238−247.

(4) Rastogi, S. K.; Bliley, J.; Shiwarski, D. J.; Raghavan, G.; Feinberg, A. W.; Cohen-Karni, T. Graphene Microelectrode Arrays for Electrical and Optical Measurements of Human Stem Cell-Derived Cardiomyocytes. *Cell. Mol. Bioeng.* **2018**, *11*, 407−418.

(5) Lee, J. H.; Kim, H.; Kim, J. H.; Lee, S.-H. Soft Implantable Microelectrodes for Future Medicine: Prosthetics, Neural Signal Recording and Neuromodulation. *Lab Chip* **2016**, *16*, 959−976.

(6) Acar, H.; Çınar, S.; Thunga, M.; Kessler, M. R.; Hashemi, N.; Montazami, R. Study of Physically Transient Insulating Materials as a Potential Platform for Transient Electronics and Bioelectronics. *Adv. Funct. Mater.* **2014**, *24*, 4135−4143.

(7) McNamara, M. C.; Aykar, S. S.; Montazami, R.; Hashemi, N. N. Targeted Microfluidic Manufacturing to Mimic Biological Microenvironments: Cell-Encapsulated Hollow Fibers. *ACS Macro Letters* **2021**, *10*, 732−736.

(8) Lim, E. L.; Yap, C. C.; Jumali, M. H. H.; Teridi, M. A. M.; Teh, C. H. A Mini Review: Can Graphene Be a Novel Material for Perovskite Solar Cell Applications? *Nano−Micro Lett.* **2018**, *10*, 27.

(9) Diemert, S.; Dolga, A. M.; Tobaben, S.; Grohm, J.; Pfeifer, S.; Oexler, E.; Culmsee, C. Impedance Measurement for Real Time Detection of Neuronal Cell Death. *J. Neurosci. Methods* **2012**, *203*, 69−77.

(10) Ali, S.; Wall, I. B.; Mason, C.; Pelling, A. E.; Veraitch, F. S. The Effect of Young's Modulus on the Neuronal Differentiation of Mouse Embryonic Stem Cells. *Acta Biomater.* **2015**, *25*, 253−267.

(11) Qiang, Y.; Seo, K. J.; Zhao, X.; Artoni, P.; Golshan, N. H.; Culaclii, S.; Wang, P.-M.; Liu, W.; Ziemer, K. S.; Fagiolini, M.; Fang, H. Bilayer Nanomesh Structures for Transparent Recording and Stimulating Microelectrodes. *Adv. Funct. Mater.* **2017**, *27*, 1704117.

(12) Gross, G. W.; Wen, W. Y.; Lin, J. W. Transparent Indium-Tin Oxide Electrode Patterns for Extracellular, Multisite Recording in Neuronal Cultures. *J. Neurosci. Methods* **1985**, *15*, 243−252.

(13) Li, H.; Liu, H.; Sun, M.; Huang, Y.; Xu, L.; Li, H.; Liu, H.; Sun, M.; Xu, L.; Huang, Y. A. 3D Interfacing between Soft Electronic Tools and Complex Biological Tissues. *Adv. Mater.* **2021**, *33*, 2004425.

(14) Fattahi, P.; Yang, G.; Kim, G.; Abidian, M. R.; Abidian, M. R.; Yang, G.; Kim, G.; Fattahi, P. A Review of Organic and Inorganic Biomaterials for Neural Interfaces. *Adv. Mater.* **2014**, *26*, 1846−1885.

(15) Adly, N.; Weidlich, S.; Seyock, S.; Brings, F.; Yakushenko, A.; Offenhäusser, A.; Wolfrum, B. Printed Microelectrode Arrays on Soft Materials: From PDMS to Hydrogels. *npj Flexible Electron.* **2018**, *2*, 1−9.

(16) Ding, X.; Liu, H.; Fan, Y. Graphene-Based Materials in Regenerative Medicine. *Adv. Healthcare Mater.* **2015**, *4*, 1451−1468.

(17) Lee, W. C.; Lim, C. H. Y. X.; Shi, H.; Tang, L. A. L.; Wang, Y.; Lim, C. T.; Loh, K. P. Origin of Enhanced Stem Cell Growth and Differentiation on Graphene and Graphene Oxide. *ACS Nano* **2011**, *5*, 7334−7341.

(18) McNamara, M. C.; Aykar, S. S.; Alimoradi, N.; Niaraki Asli, A. E.; Pemathilaka, R. L.; Wrede, A. H.; Montazami, R.; Hashemi, N. N. Behavior of Neural Cells Post Manufacturing and After Prolonged Encapsulation within Conductive Graphene-Laden Alginate Microfibers. *Adv. Biol.* **2021**, *5*, 2101026.

(19) Abdolahad, M.; Janmaleki, M.; Taghinejad, M.; Taghnejad, H.; Salehi, F.; Mohajerzadeh, S. Single-Cell Resolution Diagnosis of Cancer Cells by Carbon Nanotube Electrical Spectroscopy. *Nanoscale* **2013**, *5*, 3421−3427.

(20) Glickman, Y. A.; Filo, O.; David, M.; Yayon, A.; Topaz, M.; Zamir, B.; Ginzburg, A.; Rozenman, D.; Kenan, G. Electrical

Impedance Scanning: A New Approach to Skin Cancer Diagnosis. *Skin Res. Technol.* **2003**, *9*, 262−268.
(21) Niaraki Asli, A. E.; Guo, J.; Lai, P. L.; Montazami, R.; Hashemi, N. N. High-Yield Production of Aqueous Graphene for Electrohydrodynamic Drop-on-Demand Printing of Biocompatible Conductive Patterns. *Biosensors* **2020**, *10*, 6.
(22) Guo, J.; Niaraki Asli, A. E. N.; Williams, K. R.; Lai, P. L.; Wang, X.; Montazami, R.; Hashemi, N. N. Viability of Neural Cells on 3D Printed Graphene Bioelectronics. *Biosensors* **2019**, *9*, 112.
(23) Ahadian, S.; Estili, M.; Surya, V. J.; Ramón-Azcón, J.; Liang, X.; Shiku, H.; Ramalingam, M.; Matsue, T.; Sakka, Y.; Bae, H.; Nakajima, K.; Kawazoe, Y.; Khademhosseini, A. Facile and Green Production of Aqueous Graphene Dispersions for Biomedical Applications. *Nanoscale* **2015**, *7*, 6436−6443.
(24) Pattammattel, A.; Kumar, C. V. Kitchen Chemistry 101: Multigram Production of High Quality Biographene in a Blender with Edible Proteins. *Adv. Funct. Mater.* **2015**, *25*, 7088−7098.
(25) Paton, K. R.; Varrla, E.; Backes, C.; Smith, R. J.; Khan, U.; O'Neill, A.; Boland, C.; Lotya, M.; Istrate, O. M.; King, P.; Higgins, T.; Barwich, S.; May, P.; Puczkarski, P.; Ahmed, I.; Moebius, M.; Pettersson, H.; Long, E.; Coelho, J.; O'Brien, S. E.; McGuire, E. K.; Sanchez, B. M.; Duesberg, G. S.; McEvoy, N.; Pennycook, T. J.; Downing, C.; Crossley, A.; Nicolosi, V.; Coleman, J. N. Scalable Production of Large Quantities of Defect-Free Few-Layer Graphene by Shear Exfoliation in Liquids. *Nat. Mater.* **2014**, *13*, 624−630.
(26) Huang, L.; Huang, Y.; Liang, J.; Wan, X.; Chen, Y. Graphene-Based Conducting Inks for Direct Inkjet Printing of Flexible Conductive Patterns and Their Applications in Electric Circuits and Chemical Sensors. *Nano Res.* **2011**, *4*, 675−684.
(27) Hondred, J. A.; Breger, J. C.; Alves, N. J.; Trammell, S. A.; Walper, S. A.; Medintz, I. L.; Claussen, J. C. Printed Graphene Electrochemical Biosensors Fabricated by Inkjet Maskless Lithography for Rapid and Sensitive Detection of Organophosphates. *ACS Appl. Mater. Interfaces* **2018**, *10*, 11125−11134.
(28) Majee, S.; Song, M.; Zhang, S.-L.; Zhang, Z.-B. Scalable Inkjet Printing of Shear-Exfoliated Graphene Transparent Conductive Fi Lms. *Carbon* **2016**, *102*, 51−57.
(29) Secor, E. B.; Ahn, B. Y.; Gao, T. Z.; Lewis, J. A.; Hersam, M. C. Rapid and Versatile Photonic Annealing of Graphene Inks for Flexible Printed Electronics. *Adv. Mater.* **2015**, *27*, 6683−6688.
(30) Hashemi, N.; Lackore, J. M.; Sharifi, F.; Goodrich, P. J.; Winchell, M. L.; Hashemi, N. A Paper-Based Microbial Fuel Cell Operating under Continuous Flow Condition. *Technology* **2016**, *04*, 98−103.
(31) Kauling, A. P.; Seefeldt, A. T.; Pisoni, D. P.; Pradeep, R. C.; Bentini, R.; Oliveira, R. V. B.; Novoselov, K. S.; Castro Neto, A. H. The Worldwide Graphene Flake Production. *Adv. Mater.* **2018**, *30*, 1803784−6.
(32) Wang, Z. S.; Zhang, R.; Zhang, Z. D.; Huang, Z. H.; Liu, C. S.; Fu, D. J.; Liu, J. R. Raman Spectroscopy of Few-Layer Graphene Prepared by C2-C 6 Cluster Ion Implantation. *Nucl. Instrum. Methods Phys. Res., Sect. B* **2013**, *307*, 40−42.
(33) Fromm, J. E. Numerical Calculation Of The Fluid Dynamics Of Drop-On-Demand Jets. *IBM J. Res. Dev.* **1984**, *28*, 322−333.
(34) Derby, B.; Reis, N. Inkjet Printing of Highly Loaded Particulate Suspensions. *MRS Bull.* **2003**, *28*, 815−818.
(35) Park, D.-W.; Schendel, A. A.; Mikael, S.; Brodnick, S. K.; Richner, T. J.; Ness, J. P.; Hayat, M. R.; Atry, F.; Frye, S. T.; Pashaie, R.; Thongpang, S.; Ma, Z.; Williams, J. C. Graphene-Based Carbon-Layered Electrode Array Technology for Neural Imaging and Optogenetic Applications. *Nat. Commun.* **2014**, *5*, 1−11.
(36) Song, J.; Li, Y.; Yin, F.; Zhang, Z.; Ke, D.; Wang, D.; Yuan, Q.; Zhang, X.-E.; Zhang, X. E.; Zhang, X. E. Enhanced Electrochemical Impedance Spectroscopy Analysis of Microbial Biofilms on an Electrochemically in Situ Generated Graphene Interface. *ACS Sens.* **2020**, *5*, 1795−1803.
(37) Gao, K.; Li, L.; He, L.; Hinkle, K.; Wu, Y.; Ma, J.; Chang, L.; Zhao, X.; Perez, D. G.; Eckardt, S.; Mclaughlin, J.; Liu, B.; Farson, D. F.; Lee, L. J. Design of a Microchannel-Nanochannel-Microchannel Array Based Nanoelectroporation System for Precise Gene Transfection. *Small* **2014**, *10*, 1015−1023.
(38) Gifford, S. C.; Frank, M. G.; Derganc, J.; Gabel, C.; Austin, R. H.; Yoshida, T.; Bitensky, M. W. Parallel Microchannel-Based Measurements of Individual Erythrocyte Areas and Volumes. *Biophys. J.* **2003**, *84*, 623−633.
(39) Bai, Z.; Mendoza Reyes, J. M.; Montazami, R.; Hashemi, N. On-Chip Development of Hydrogel Microfibers from Round to Square/Ribbon Shape. *J. Mater. Chem. A* **2014**, *2*, 4878−4884.
(40) Sharifi, F.; Patel, B. B.; Dzuilko, A. K.; Montazami, R.; Sakaguchi, D. S.; Hashemi, N. Polycaprolactone Microfibrous Scaffolds to Navigate Neural Stem Cells. *Biomacromolecules* **2016**, *17*, 3287−3297.

https://doi.org/10.1021/acsabm.1c00913
ACS Appl. Bio Mater. 2022, 5, 113−122